Supplementary Information: Activity-driven tissue alignment in proliferating spheroids

Liam J. Ruske and Julia M. Yeomans
Rudolf Peierls Centre For Theoretical Physics, University of Oxford, Parks Road, Oxford OX1 3PU, UK
(Dated: December 22, 2022)

I. EXPRESSIONS FOR THE FREE ENERGY AND HYDRODYNAMIC EQUATIONS OF MOTION

Rod-like particles can not only be advected by the fluid, but also rotate in response to flow gradients. This behaviour is accounted for by the co-rotational term [1]

$$\mathcal{W}_{ij} = \left(\xi\tilde{E}_{ik} + \Omega_{ik}\right)\left(Q_{kj} + \frac{\delta_{kj}}{3}\right) + \left(Q_{ik} + \frac{\delta_{ik}}{3}\right)\left(\xi\tilde{E}_{kj} - \Omega_{kj}\right) - 2\xi\left(Q_{ij} + \frac{\delta_{ij}}{3}\right)Q_{kl}W_{lk}\,, \quad (1)$$

where $\tilde{E}_{ij} = E_{ij} - \delta_{ij}E_{kk}/3$ is the traceless part of the strain rate tensor $E_{ij} = (\partial_j u_i + \partial_i u_j)/2$ and $\Omega_{ij} = (\partial_j u_i - \partial_i u_j)/2$ is the antisymmetric part of the velocity gradient tensor $W_{ij} = \partial_i u_j$. The alignment parameter ξ quantifies how the director responds to pure shear flow.

The passive contributions of the hydrodynamic stress tensor $\Pi_{passive}$ in the Navier-Stokes equations are

$$\Pi_{viscous} = 2\eta\mathbf{D}\,, \quad (2)$$

$$\Pi_{capillary} = (f - \mu\varphi)\mathbf{I} - \nabla\varphi\left(\frac{\partial f}{\partial(\nabla\varphi)}\right) + \nabla\varphi\nabla\left(\frac{\partial f}{\partial(\nabla^2\varphi)}\right) - \nabla\nabla\varphi\left(\frac{\partial f}{\partial(\nabla^2\varphi)}\right)\,, \quad (3)$$

$$\Pi_{elastic} = -p\mathbf{I} - \xi[\mathbf{H}\tilde{\mathbf{Q}} + \tilde{\mathbf{Q}}\mathbf{H} - 2\tilde{\mathbf{Q}}tr(\mathbf{QH})] + \mathbf{QH} - \mathbf{HQ} - \nabla\mathbf{Q}\left(\frac{\partial f}{\partial(\nabla\mathbf{Q})}\right)\,, \quad (4)$$

where ρ is the density, η the viscosity, p the bulk pressure and $\tilde{\mathbf{Q}} = \left(\mathbf{Q} + \frac{1}{3}\mathbf{I}\right)$. The free energy density $f = f_{LC} + f_{GL}$ consists of a liquid crystal component f_{LC} for the orientational order parameter $\mathbf{Q}$ and a Ginzburg-Landau contribution f_{GL} for a concentration field φ which is described below.

The mechanical and geometric properties of cells are accounted for by choosing an appropriate nematic free energy density of the system

$$f_{LC} = A_{LC}\left\{\frac{1}{2}\left(1 - \frac{\bar{\eta}(\varphi)}{3}\right)\mathrm{tr}(\mathbf{Q}^2) - \frac{\bar{\eta}(\varphi)}{3}\mathrm{tr}(\mathbf{Q}^3) + \frac{\bar{\eta}(\varphi)}{4}\mathrm{tr}(\mathbf{Q}^2)^2\right\} + \frac{1}{2}K_{LC}\left(\nabla\mathbf{Q}\right)^2 \quad (5)$$

which includes the usual Landau-de Gennes bulk energy of the liquid crystal and a term which penalizes elastic deformations of the director field [2].

We follow the shape of the growing spheroids by modelling them as deformable, nematic droplets in an isotropic fluid background. This is achieved by solving the reaction-diffusion equation of a concentration field $\varphi(\mathbf{x}, t)$, as described in detail in previous work [3]:

$$\left(\partial_t + \mathbf{u}\cdot\nabla\right)\varphi = \Gamma_\varphi\,\nabla^2\mu\,. \quad (6)$$

Here $\mathbf{u}$ is the velocity field and the mobility Γ_φ quantifies how fast φ responds to gradients in the chemical potential $\mu = \delta\mathcal{F}/\delta\varphi$. The free energy density f_{GL} is chosen to take the Ginzburg-Landau form

$$f_{GL} = A_\varphi\varphi^2\left(1-\varphi\right)^2 + \frac{K_\varphi}{2}\left(\nabla\varphi\right)^2\,. \quad (7)$$

This describes phase separation into two stable phases with concentrations $\varphi = 0, 1$ and with an interface of width $L \sim \sqrt{K_\varphi/A_\varphi}$ which separates the inside ($\varphi = 1$) and outside ($\varphi = 0$) of spheriods and introduces a surface tension $\gamma \sim \sqrt{A_\varphi K_\varphi}$ [4]. Parameters A_φ and K_φ are chosen to match the surface tension γ measured in experiments, while ensuring that the interface width is much smaller than any other length-scale in the system, $L \ll \min[\ell_a, \ell_m]$. Since cell aggregates are modelled using a continuous concentration field $0 \leq \varphi \leq 1$, the net cell production rate and active stress in simulations are continuous functions and follow $k_p^{LB} = \varphi\, k_p$ and $\zeta^{LB} = \varphi\,\zeta$, respectively (see Fig. S2).

Throughout the paper we use the following simulation parameters, in lattice-units, unless otherwise stated: $\rho = 1$, $\eta = 2/3$, $A_\varphi = 0.2$, $K_\varphi = 0.4$, $\Gamma_\varphi = 0.2$, $A_{LC} = 1.5$, $K_{LC} = 0.03$, $\Gamma = 0.1$. To highlight the effects of flow-induced elongation of isotropic cells in section III A, we chose $\bar{\eta} = 2.55 + 0.1\varphi$ which creates an isotropic phase $S_{eq} = 0$ inside droplets unless flows drive nematic order for $\xi \neq 0$. In sections III B-D, we chose $\bar{\eta} = 2.7 + 0.3(\varphi - 0.5)$ which creates nematic order $S_{eq} = 0.3$ of constant magnitude inside aggregates ($\varphi = 1$), while ensuring that the fluid environment stays isotropic ($\varphi = 0$).

II. STABILITY ANALYSIS OF ISOTROPIC SPHEROIDS

We derive the stability of the isotropic state $Q_{ij} = 0 + Q'_{ij}$ by expanding the Beris-Edwards equation to first

order in perturbation parameter $Q'_{ij} = \epsilon(n_i n_j - \delta_{ij}/3)$,

$$D_t Q'_{ij} - \mathcal{W}_{ij} = \Gamma K_{LC} \left(\partial_k \partial_k Q'_{ij}\right) + \mathcal{O}(\epsilon^2) \,. \quad (8)$$

Following eqn. (1), the leading order contribution of the co-rotation term $\mathcal{W}_{ij}$ is

$$\mathcal{W}_{ij} = \frac{2}{3}\xi \tilde{E}_{ij} + \mathcal{O}(\epsilon) \,, \quad (9)$$

where we have used the symmetry of $\tilde{E}_{ij}$ and Q'_{ij}. The stability of the isotropic state is thus governed by

$$\dot{Q}_{ij} = \frac{2}{3}\xi \left(E_{ij} - \delta_{ij}\frac{E_{kk}}{3}\right) + \mathcal{O}(\epsilon) \,, \quad (10)$$

where we have neglected the advective term, $u_k \partial_k Q_{ij}$, since spatial gradients $\nabla \mathbf{Q}$ vanish in the isotropic state. In spherical coordinates the strain rate tensor $E_{ij} = (\partial_j u_i + \partial_i u_j)/2$ has components

$$E_{rr} = \partial_r u_r \,, \quad (11)$$

$$E_{\theta\theta} = E_{\phi\phi} = \frac{u_r}{r} \,, \quad (12)$$

$$E_{r\theta} = E_{r\phi} = E_{\theta\phi} = 0 \,, \quad (13)$$

where we have used the symmetry of the flow field $\mathbf{u}(r, \theta, \phi) = u_r(r)\hat{\mathbf{r}}$. This yields the initial growth rate of the radial component of the nematic order

$$\dot{Q}_{rr} = \frac{4}{9}\xi \left(\partial_r u_r - \frac{u_r}{r}\right) \,. \quad (14)$$

III. MAPPING OF SIMULATION PARAMETERS TO EXPERIMENTAL VALUES

In order to map lattice Boltzmann (LB) simulation parameters to dimensional quantities in physical units, one requires a physical reference scale for three independent LB parameters, such as the lattice spacing δx, a force scale and the viscosity. For modelling the organisation of three-dimensional, multicellular spheroids, we chose a lattice spacing such that the total diameter of an aggregate is about 50 lattice sites, $\delta x \approx 0.04\, R$. To estimate the bending rigidity of cells K_{LC} in experiments, we need to relate the mechanical properties of individual cells to the effective constant K_{LC} of the nematic description. If we assume that cells in a dense aggregate must physically deform when the nematic order is distorted, the elastic energy associated with cell shape deformations is related to the cells' Young modulus E and cell size L. From dimensional arguments, it follows that $K_{LC} \sim E \cdot L^2$ [5]. The typical size and Young's modulus of colon and breast cancer cell lines is of the order of $L \sim 10\,\mu m$ and $E \sim 100\,Pa$ [6–8], respectively, which yields $K_{LC} \sim 10^{-8} N$. Choosing $K_{LC} = 5 \cdot 10^{-8} N$ and the apparent viscosity of cell aggregates $\eta \approx 60\, kPa\, s$ [9, 10] as LB reference scales, the LB parameters map to the following physical units:

Parameter	LB units	Physical units
Aggregate size R	25	$300\,\mu m$
Bending rigidity K_{LC}	0.03	$5 \cdot 10^{-8}\, N$
Viscosity η	2/3	$60\, kPa\, s$
Lattice spacing δx	1	$12\,\mu m$
Time step δt	1	$15\, s$
Critical concentration m_c	0.8	0.8
Penetration length ℓ_M	12	$150\,\mu m$
Growth rate k_p	$8 \cdot 10^{-4}$	$5 \cdot 10^{-5}\, s^{-1}$
Active stress ζ	$0.005 - 0.04$	$30 - 240\, Pa$
Surface tension γ	0.3	$4 \cdot 10^{-2}\, N/m$
Spheroid bulk energy A_φ	0.2	$2.4\, kPa$
Nematic bulk energy A_{LC}	1.5	$18\, kPa$
Rotational diffusivity Γ	0.1	$6 \cdot 10^{-7}\, (Pa\, s)^{-1}$
Mobility Γ_φ	0.2	$8 \cdot 10^{-16}\, m^2/Pa\, s$

As outlined in section III D, these parameters are in good agreement with mechanical properties of cell aggregates measured in experiments, with typical tissue interfacial tensions $\gamma \sim 10^{-2}\, N/m$ [9, 11–13]. It should be noted, however, that the mechanical properties of cell aggregates may vary greatly as the Young's modulus varies over several orders of magnitude, $E \sim 0.1{-}10 kPa$ for different cell types [14, 15]. Similar variations are observed for the effective viscosity of tissues and cell aggregates, $\eta \sim 10 - 100\, kPa\, s$ [11, 12, 16].

IV. DETECTION OF DISCLINATION LINES AND CALCULATION OF THE TWIST ANGLE β

We use Zapotoky's defect-finding algorithm [17] to find defect positions on three-dimensional grids. This approach checks if a disclination is located at the intersection of four voxels forming a 2×2 square repeated along all three coordinate axis [18]. When a disclination is found, the rotation vector Ω along which the director field winds is determined by taking the cross product of each pair of directors around it. Once all grid points are classified, continuous disclination lines are identified as the shortest line connecting all defect positions, and the twist-angle β can be obtained by measuring the angle between Ω and the local line tangent. A shortcoming of this algorithm is that the rotation vector Ω has an arbitrary sign and therefore is unsuited to distinguishing between $\beta = 0$ ($-1/2$-type) and $\beta = \pi$ ($+1/2$-type) disclinations. To achieve this, we calculate the saddle-splay energy

$$\bar{f}_{24} = \nabla \cdot [(\mathbf{n} \cdot \nabla)\mathbf{n} - \mathbf{n}(\nabla \cdot \mathbf{n})] \,, \quad (15)$$

which is negative for $\beta = \pi$ line segments, positive at $\beta = 0$ segments and zero for twist defects [19]. The calculation of the line tangent is performed on a discrete grid, hence the local tangent does not vary continuously along disclination lines which leads to the small color jumps seen for some disclination line segments in Fig. S3 and Fig. S4.

V. SUPPLEMENTARY FIGURES

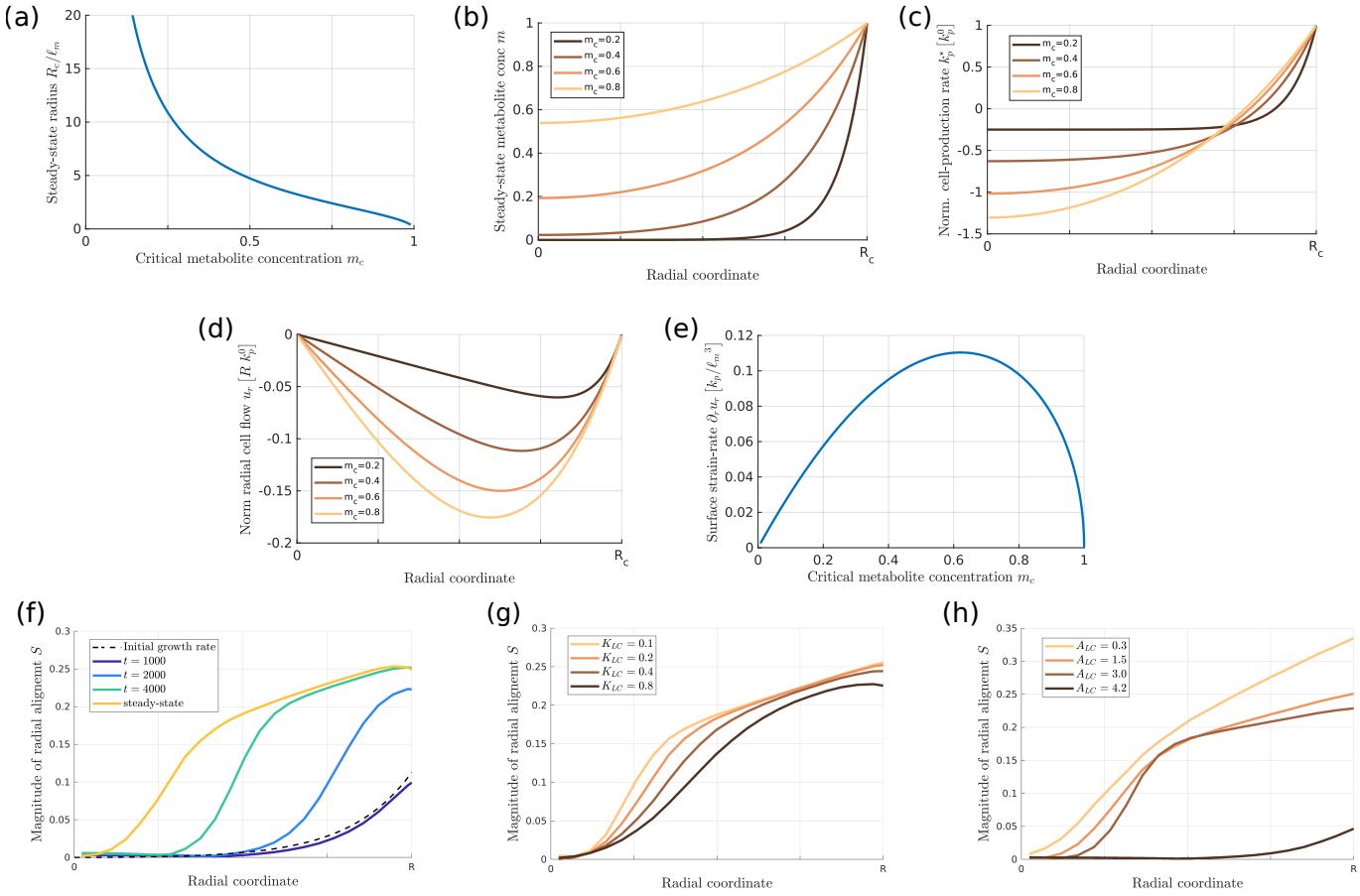

FIG. S1. **(a)** Steady-state radius R_c/ℓ_m as a function of critical metabolite concentration m_c. **(b-e)** In steady-state spheroids the critical concentration m_c controls the shape of the radial metabolite profile m (panel b), cell production profile $k_p^\star$ (panel c) and flow profile u_r (panel d). The cell production rate $k_p^\star$ and cell flow u_r are normalized to the cell production rate at the surface, $k_p^0 = k_p(1 - m_c)$. **(e)** The strain rate at the surface of spheroids, which drives flow-induced cell elongation, scales as $\partial_r u_r \sim k_p \ell_m^{-3}$ and reaches a maximum value at $m_c \approx 0.6$. **(f)** Time-evolution of the radial cell alignment $Q_{rr} \sim S$ in numerical simulations initialized as $S = 0$ with $\xi > 0$. Initially S follows the linear growth rate shown by eqn. (13) in the main text (black, dashed line). At late times, however, non-linear contributions arising from advection and the molecular field $\mathbf{H}$ balance the growth rate and S reaches a steady-state profile (yellow line). **(g,h)** Numerical cell alignment profiles at steady-state for different values of cell parameters A_{LC} and K_{LC}. Simulations were performed with spheroids of size $R = 30$ using isotropic cells ($S_{eq} = 0$) and $k_p = 0.001$, $\xi = 0.3$.

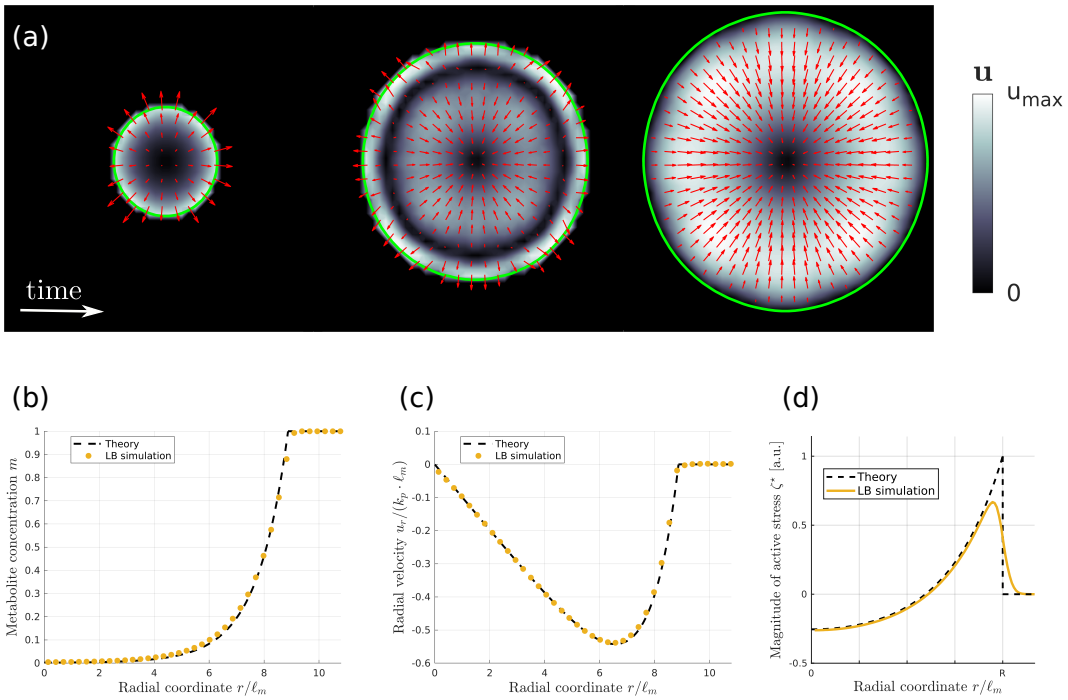

FIG. S2. **(a)** Snapshots showing the time evolution of the velocity field $\mathbf{u}$ inside a growing cell aggregate ($\zeta = 0$) using the hybrid lattice Boltzmann-finite difference method. At early times the spheroid is in a growing state $\dot{R} > 0$ because sufficient metabolites are available throughout the aggregate, $m(r) > m_c$, creating diverging cell flows $u_r > 0$. As the aggregate size increases, cells in the core will eventually have insufficient access to metabolites, $m(r = 0) < m_c$, resulting in converging cell flows $u_r < 0$ towards the centre. Spheroids will finally reach a steady state in which cell division and death exactly balance, $\dot{R} = 0$, leading to $u_r < 0$ throughout the aggregate. Snapshots show the cross-section at the equator of a growing spheroid defined by a concentration field φ (see appendix I), where the boundary of the aggregate is marked by the contour $\varphi = 0.5$ (green line). **(b-d)** Comparison between metabolite concentration m, velocity field u_r and active stress $\zeta^\star$ obtained in lattice Boltzmann simulations (orange) and analytical solutions (black, dotted line) following eqns. (9, 11) in the main text. We validated that in the absence of sources and sinks in the continuity equation, $\nabla \cdot \mathbf{u} = 0$, the flow fields obtained from the lattice-Boltzmann solver remain incompressible, with density fluctuations $\delta\rho/\rho < 0.03$.

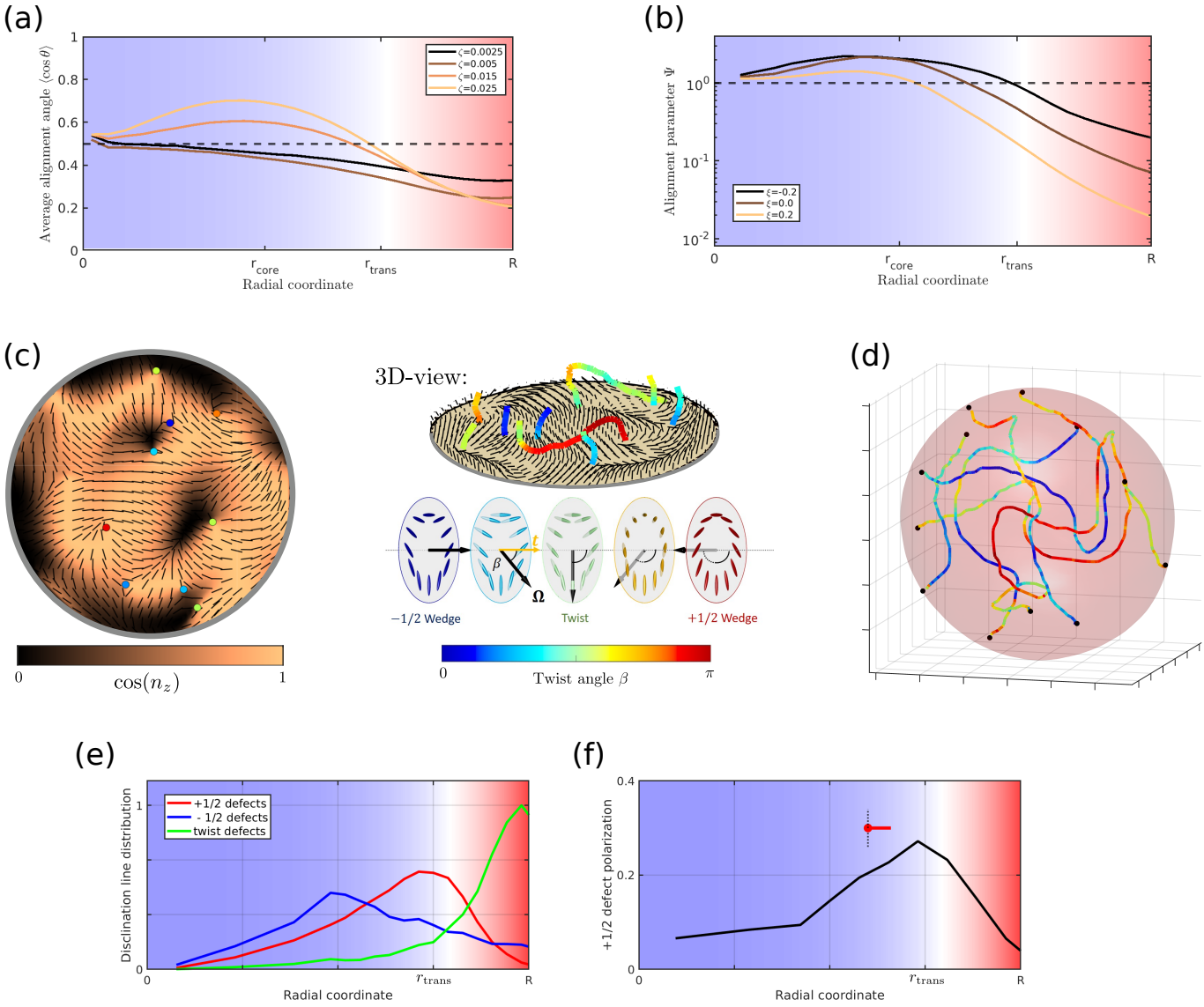

FIG. S3. **(a)** Cell alignment quantified by the average alignment angle $\langle \cos\theta \rangle$ as a function of radial coordinate for different magnitudes of active stress ζ. The data is identical to that used in Fig. 2 e in the main text. **(b)** Cell alignment Ψ for different values of alignment parameter ξ. All other parameters are identical to the ones used in Fig. 2. **(c)** In two-dimensional cross-sections of the 3D director field inside active spheroids one can identify topological defects as points where the nematic director field discontinuously changes its direction. If the director field around a defect has no out-of-plane component, $n_z = 0$, it is called a wedge-type disclination and resembles $\pm 1/2$ defects in 2D systems. If the out-of-plane component n_z significantly varies around a defect it is called a twist-type disclination. Disclination lines in three dimensions can continuously transform from a local $-1/2$ configuration (in the plane perpendicular to the line) into a $+1/2$ configuration through an intermediate twist winding. Disclination lines can be locally classified by the *twist-angle* β between the axis $\mathbf{\Omega}$ that the director field winds around and the local line tangent $\mathbf{t}$ (yellow arrow). **(d)** Due to activity disclination lines act as self-propelled entities moving through the fluid leading to spatiotemporally chaotic flows. Disclination lines constantly undergo transformation events such as breakup, recombination, nucleation and annihilation and form either closed, charge-neutral loops in the bulk or terminate at the surface of droplets. **(e)** The distribution of disclination types follows the activity profile $\zeta^\star \sim (m - m_c)$, where contractile regions in the core are dominated by wedge-type $\pm 1/2$ disclinations and twist-type defects are preferentially formed in extensile regions close to the surface. **(f)** Activity gradients in the aggregate create active torques on $+1/2$ defects which aligns them parallel to activity gradients, where the head-to-tail vector $\mathbf{p} \sim \nabla\zeta^\star$. Using a polarization order parameter $\mathcal{P}$ [20] to quantify the magnitude of defect alignment, we find that $+1/2$ defects are radially polarized throughout the aggregate. The polarization order parameter $\mathcal{P}$ reaches a maximum at the radius $r \approx r_{\text{trans}}$, where $\zeta^\star \approx 0$ and activity gradients dominate isotropic active turbulence, $\mathbf{Q}\nabla\zeta^\star > \zeta^\star\nabla\mathbf{Q}$. This is also reflected in the radial defect distribution in (c), where radially polarized $+1/2$ defects move outwards/inwards in contractile/extensile regions, thus accumulating around $r \approx r_{\text{trans}}$. Numerical details of the detection of disclination lines and the calculation of the twist angle β are outlined in appendix IV.

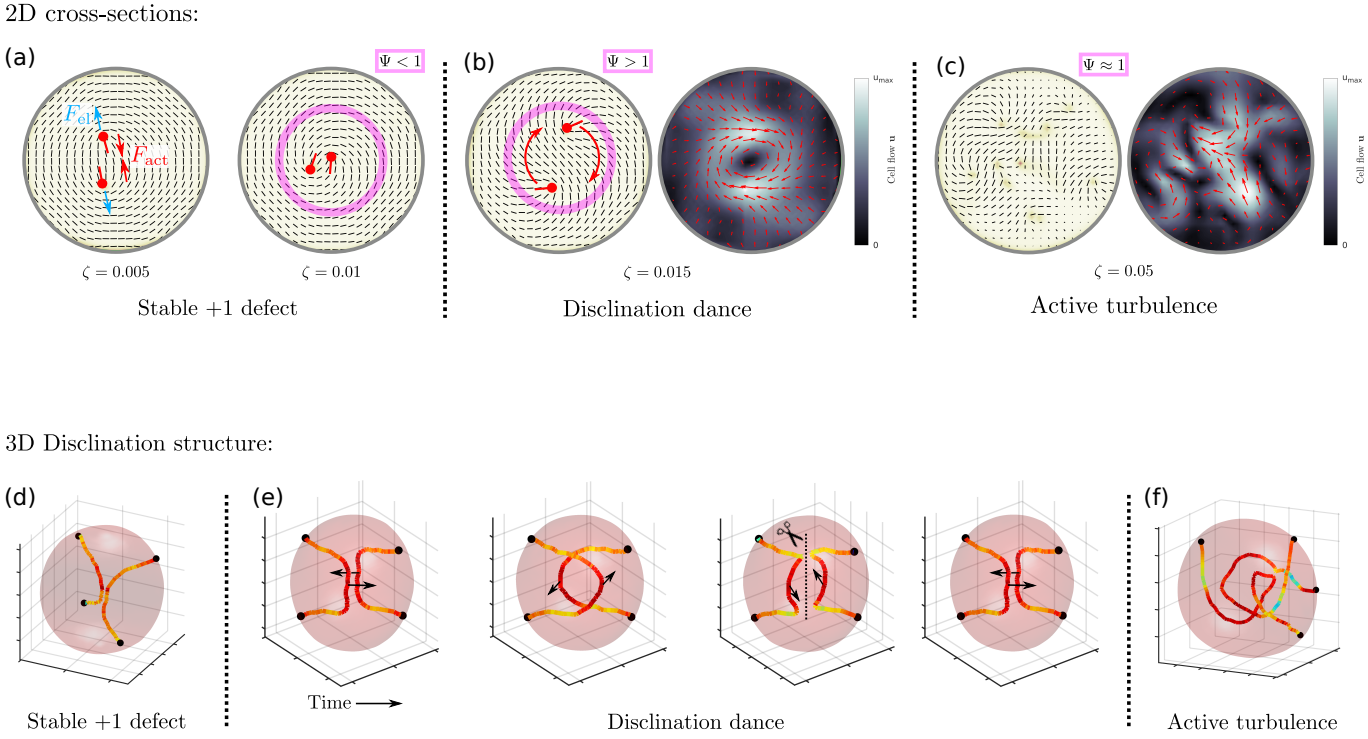

FIG. S4. As the activity ζ is progressively increased inside proliferating spheroids with $\xi < 0$, the droplet undergoes three dynamical regimes: first a quiescent regime where converging flows are dominant (a,d), then a rotational *dancing disclination* regime, where disclination lines spontaneously set up a rotational flow and, finally, active turbulence. **(a,d)** Two-dimensional cross-sections of the director field and disclination line structure. At very low activity the director field is stationary and the 2D cross-section resembles a +1 defect with angular director alignment ($\Psi < 1$), where two +1/2 defects are located at a small finite distance to the centre. Contractile stress around defects creates active forces F_{act} pointing towards the centre (red). If activity is sufficient small, active forces are balanced by repulsive elastic forces F_{el} (blue) arising from an increased elastic energy as the distance between +1/2 defects decreases. **(b,e)** If activity surpasses a critical threshold ζ_c, the system reaches a steady-state where the two +1/2 disclination lines start orbiting around each other, thereby creating persistent rotational motion in the core of spheroids, as shown by the cross-section of the velocity field. The outward-facing orientation of the defects creates significant radial alignment of the director field in the vicinity of the orbiting defects ($\Psi > 1$). The rotational motion of defects in the core makes it inevitable that disclination lines must cross after each full rotation, thereby rewiring some line segments (see third panel in e). **(c,f)** As activity progressively increases, the motion of disclination lines and flow fields becomes more chaotic and the system eventually reaches active turbulence. The snapshots shown in this figure were obtained for $\xi = -0.4$ and disclination lines are coloured according to their local twist-angle β using the color map shown in Fig. S3.

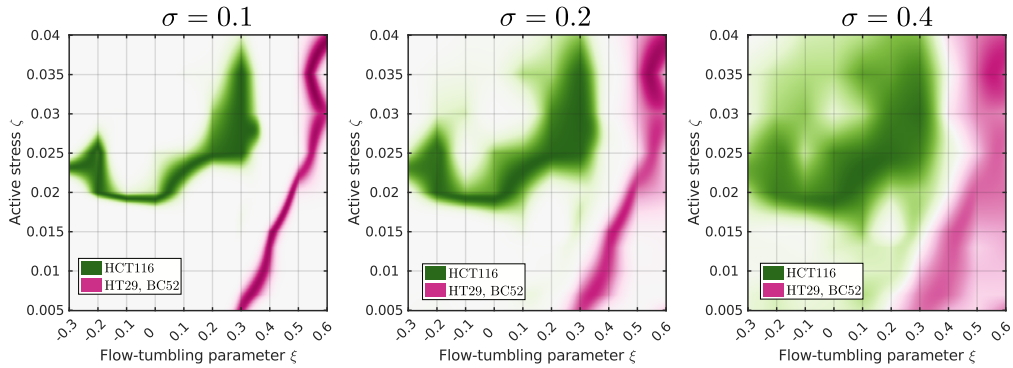

FIG. S5. Posterior distributions $p(\Theta|\mathbf{X})$ over model parameters $\Theta = [\zeta, \xi]$ given data $\mathbf{X} = [\Psi_s^{exp}, \Psi_c^{exp}]$ for different tolerance values σ. The variance of posterior distributions increases with larger tolerance, but the mode of the distributions remains the same.

[1] Beris AN, Edwards BJ. Thermodynamics of flowing systems with internal microstructure. 36. Oxford University Press; 1994.

[2] De Gennes PG, Prost J. The Physics of Liquid Crystals. vol. 83. Oxford University Press; 1993.

[3] Ruske LJ, Yeomans JM. Morphology of active deformable 3D droplets. Physical Review X. 2021;11(2):021001.

[4] Cahn JW, Hilliard JE. Free energy of a nonuniform system. I. Interfacial free energy. The Journal of Chemical Physics. 1958;28(2):258–267.

[5] Duclos G, Garcia S, Yevick H, Silberzan P. Perfect nematic order in confined monolayers of spindle-shaped cells. Soft Matter. 2014;10(14):2346–2353.

[6] Pachenari M, Seyedpour SM, Janmaleki M, Shayan SB, Taranejoo S, Hosseinkhani H. Mechanical properties of cancer cytoskeleton depend on actin filaments to microtubules content: investigating different grades of colon cancer cell lines. Journal of Biomechanics. 2014;47(2):373–379.

[7] Li Q, Lee GY, Ong CN, Lim CT. AFM indentation study of breast cancer cells. Biochemical and Biophysical Research Communications. 2008;374(4):609–613.

[8] Nematbakhsh Y, Pang KT, Lim CT. Correlating the viscoelasticity of breast cancer cells with their malignancy. Convergent Science Physical Oncology. 2017;3(3):034003.

[9] Forgacs G, Foty RA, Shafrir Y, Steinberg MS. Viscoelastic properties of living embryonic tissues: a quantitative study. Biophysical Journal. 1998;74(5):2227–2234.

[10] Duclut C, Sarkar N, Prost J, Jülicher F. Fluid pumping and active flexoelectricity can promote lumen nucleation in cell assemblies. Proceedings of the National Academy of Sciences. 2019;116(39):19264–19273.

[11] Stirbat TV, Mgharbel A, Bodennec S, Ferri K, Mertani HC, Rieu JP, et al. Fine tuning of tissues' viscosity and surface tension through contractility suggests a new role for α-catenin. PLoS One. 2013;8(2):e52554.

[12] Guevorkian K, Colbert MJ, Durth M, Dufour S, Brochard-Wyart F. Aspiration of biological viscoelastic drops. Physical Review Letters. 2010;104(21):218101.

[13] Mgharbel A, Delanoë-Ayari H, Rieu JP. Measuring accurately liquid and tissue surface tension with a compression plate tensiometer. HFSP Journal. 2009;3(3):213–221.

[14] Blumlein A, Williams N, McManus JJ. The mechanical properties of individual cell spheroids. Scientific Reports. 2017;7(1):1–10.

[15] Kuznetsova TG, Starodubtseva MN, Yegorenkov NI, Chizhik SA, Zhdanov RI. Atomic force microscopy probing of cell elasticity. Micron. 2007;38(8):824–833.

[16] Marmottant P, Mgharbel A, Käfer J, Audren B, Rieu JP, Vial JC, et al. The role of fluctuations and stress on the effective viscosity of cell aggregates. Proceedings of the National Academy of Sciences. 2009;106(41):17271–17275.

[17] Zapotocky M, Goldbart PM, Goldenfeld N. Kinetics of phase ordering in uniaxial and biaxial nematic films. Physical Review E. 1995;51(2):1216.

[18] Hobdell J, Windle A. A numerical technique for predicting microstructure in liquid crystalline polymers. Liquid Crystals. 1997;23(2):157–173.

[19] Tran L, Lavrentovich MO, Beller DA, Li N, Stebe KJ, Kamien RD. Lassoing saddle splay and the geometrical control of topological defects. Proceedings of the National Academy of Sciences. 2016;113(26):7106–7111.

[20] Ruske LJ, Yeomans JM. Activity gradients in two- and three-dimensional active nematics. Soft Matter. 2022;18(30):5654–5661.